Kinetics and Mechanism of Gold Dendrite Electroformation on C(0001). Activation Energy for Gold Adatom Surface Diffusion

H. Martín, P. Carro, A. Hernández Creus, and S. González

Departamento de Química Física, Universidad de La Laguna, La Laguna, Tenerife, Spain

R. C. Salvarezza and A. J. Arvia*

Instituto de Investigaciones Fisicoquímicas Teóricas y Aplicadas (INIFTA), Sucursal 4, Casilla de Correo 16, (1900) La Plata, Argentina

Received: June 19, 1998; In Final Form: February 10, 1999

Au electrodeposition on C(0001) from aqueous solutions with different concentrations of $AuCl_3$·HCl, at a constant ionic mass transport rate (j_L), in the temperature range $275 \leq T \leq 313$ K, results in the initial formation of nanometer-sized Au islands consisting of a central core and symmetrically distributed branches with the island fractal dimension $D_f = 1.6$. For all values of T, the time dependence of the Au island radius fulfills a $r \propto t^n$ relationship with $n = 0.25 \pm 0.05$. At constant T, the density of Au islands (N_s) increases according to $N_s \propto j_L{}^X$ with $X = 0.69 \pm 0.03$. At constant j_L, the value of N_s decreases as T is increased, following an Arrhenius-type relationship. Kinetic data are consistent with a growth mechanism involving surface diffusion of Au adatoms from the island core towards branch tips. From the dependence of N_s on T at constant j_L, the activation energy for Au adatom surface diffusion results in $E_a^* \approx 11$ Kcal/mol. This figure is slightly smaller than $E_a^* \approx 14$ Kcal/mol that has been reported for Au atom surface diffusion in Cl^--ion free acid solutions.

1. Introduction

The epitaxial growth of a solid phase on well-defined crystalline foreign substrate occurring far from equilibrium is a complex process in which different steps can be distinguished, namely, the initial formation of nuclei, nucleus growth forming two-dimensional (2D) or three-dimensional (3D) crystals, and finally, the overlapping of these crystals covering the substrate.[1] The first and second steps lead to a surface consisting of patches of the substrate and islands of the new solid phase. Under certain experimental conditions, islands can be described as strongly disordered fractal patterns.[2] The characteristics of these patterns are determined by the kinetics and mechanism of the growth process as can be concluded by comparing them to those resulting from different growth models.

The initial stages of island growth have been described by different growth models, in particular, the deposition, diffusion, and aggregation (DDA) model.[1] For the DDA model, particles deposited on the substrate are incorporated into island edges, and those deposited on islands diffuse downward to be incorporated into island edges. Patterns resulting from this model consist of 2D islands, their shape resembling closely that expected from either diffusion-limited aggregation (DLA),[3] or dendrite-like,[4] or dense radial aggregation models,[1] depending on subtle differences in the surface diffusion characteristics of arriving particles. The DDA model, although developed as a homoepitaxial model, generates growth patterns closely comparable to those resulting from heteroepitaxial experimental systems. This is the case, for instance, of DLA-like quasi-2D Au islands produced from vapor deposition on Ru(0001) at 298 K,[2] although Ag and Pt dendritic islands are formed on Pt(111) from vapor deposition at 130 K[4] and 200 K,[5] respectively. The stability of dendrite tips has been attributed to the anisotropic corner diffusion of depositing adatoms.[4,5] Furthermore, for Cu vapor-deposited on Ni(100) in the range 250−370 K, the transition from compact to branched growth has been attributed to strain relief.[6]

Transmission electron microscopy and diffraction data[7,8] on vapor-deposited Au on C(0001) grown far from equilibrium have shown initially a pseudomorphic growth that has been followed by the development of epitaxially grown branched islands. In this case, it has been observed that the increase in substrate temperature tends to change the growth mode from branching into compact islands. This change in morphology has been related to the enhancement of edge adatom diffusion.[1,4] The equilibrium shape of Au crystals on C(0001) has only been observed after annealing for 70 h at 1273 K,[9] turning the use of classical thermodynamic growth models[10] for this system inapplicable. Recently, it has been found that, under certain experimental conditions, Au electrodeposition on C(0001) from acid aqueous electrolyte solutions at 298 K[11] initially produces three-dimensional (3D) Au(111) islands followed by quasi-2D dendritic branching. In our knowledge this was the first evidence of quasi-2D nanometer-sized dendritic island formation by electrochemical deposition. In this case, the electrodeposition process is under mass transport control and it occurs in a potential (E) window that is located negatively with respect to the potential of zero charge (E_{pzc}) of Au(111) in the solution. The origin of the dendritic growth mode has been related to the existence of step edge energy barriers and anisotropic corner diffusion of Au adatoms.[4,5]

This work focuses on the kinetics and mechanism of Au dendritic growth on C(0001) by electrodeposition, in the range

* To whom all correspondence should be addressed.

10.1021/jp982695k CCC: $18.00
Published on Web 04/24/1999

$275 \leq T \leq 313$ K. Kinetic data allow us to conclude that Au surface atom diffusion plays a key role as rate-determining step in Au dendritic growth. The activation energy for Au adatom surface diffusion (E_a*) on Au resulting from the flux and temperature dependences of Au island density is $E_a^* \approx 11$ Kcal/mol. The existence of anisotropic energy barriers at step edges and anisotropic corner diffusion can explain the change in the Au island shape from quasi-2D compact to dendritic.

2. Experimental Section

The electrodeposition of Au was made in the range $275 \leq T \leq 313$ K on a freshly exfoliated C(0001) working electrode (0.5 cm^2) using a conventional glass-made electrochemical cell provided with a Pt polycrystalline counter electrode, and a saturated calomel electrode (SCE) as reference. The value of the reference electrode potential at each T was calculated using the following equation:[12]

$$E = 0.2412 - 6.61 \times 10^{-4}\,(T - 298) - 1.75 \times 10^{-6}\,(T - 298)^2 \quad (1)$$

Potentials in the text are referred to the SCE scale at $T = 298$ K.

The composition of aqueous working solutions was c $AuCl_3$·HCl + 0.5 M $NaClO_4$ + 1×10^{-2} M $HClO_4$ + 0.92×10^{-2} M NaCl, with c varied in the range 5×10^{-5} M $\leq c \leq 5 \times 10^{-4}$ M. These solutions were prepared from analytical reagent-grade chemicals and MilliQ*-Millipore water, and deaerated by bubbling purified Ar prior to Au electrodeposition. The formation of Au islands was investigated by combining electrochemical techniques and ex situ scanning tunneling microscopy (STM).

Cathodic polarization curves covering the range $0.9 \geq E \geq -0.1$ V were made with a PAR instrument consisting of EQ&G 173, 175, 178, and 179 units, at the potential scan rate $v = 1 \times 10^{-3}$ V/s to approach free convection electrodeposition under quasi-steady-state conditions. These curves provided information about the kinetics of Au electrodeposition on C(0001), and allowed us to select the most convenient potential range to produce Au dendritic islands. In the range of c and T used in this work, runs were made at constant current density in the range $40 \leq j_L \leq 140$ $\mu A/cm^2$, and electrodeposition charge density (q) in the range $0.6 \leq q \leq 25$ mC/cm^2. Both j_L and q are referred to the initial substrate surface area.

For ex situ STM imaging, the working electrode was removed from the electrochemical cell, rinsed by successive immersions in water, and finally, dried under Ar at room temperature. Immediately afterwards STM images were obtained using Nanoscope II E STM (Digital Instruments, Santa Barbara, CA) with Pt−Ir nanotips operating in air. This operation mode was feasible because of the stability of the electrode surface in air. Images were taken at 0.5 nA tunneling current, 0.2 V bias voltage, and scan rates usually in the order of 0.5 Hz for images 10×10 μm^2 in size. For these conditions, either damage to or removal from the substrate of Au crystals by the tip could be prevented.

Au electrodeposits remained unaltered after STM imaging, as was concluded for each electrode by the coincidence of the values of q determined from Au anodic stripping voltammetry before and after STM imaging.

3. Results

3.1. Cathodic Polarization Curves. The current density (j) vs potential (E) plots for Au electrodeposition on C(0001), run at $v = 0.001$ V/s starting from $E = 0.9$ V in the negative direction (Figure 1), exhibit a net cathodic current for $E < 0.72$ V in the range $275 \leq T \leq 313$ K. The initial cathodic current is related to the nucleation of Au on defective sites of C(0001) according to the following reaction:[11]

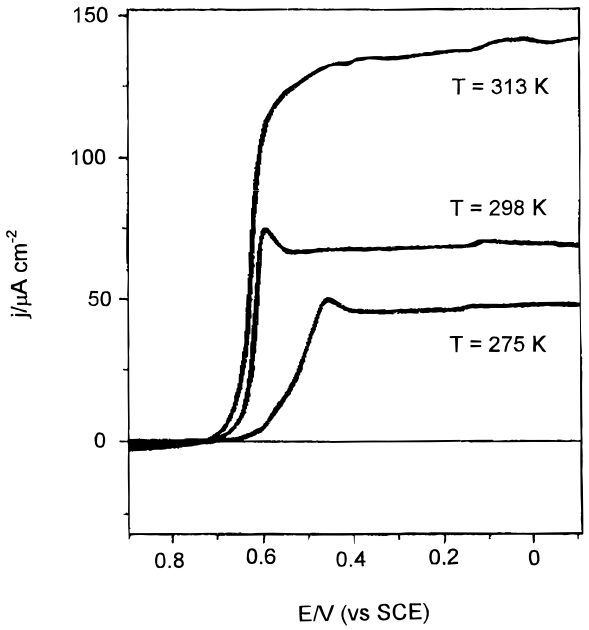

Figure 1. Current/potential curves for gold electrodeposition from aqueous 5×10^{-4} M $AuCl_3$·HCl + 0.5 M $NaClO_4$ + 0.01M $HClO_4$ on C(0001) made at 0.001 V/s and different temperatures. A clear cathodic current plateau for $E < 0.4$ V can be observed.

$$C(0001) + m AuCl_4^- + 3me^- = C(0001)\{Au\}_m + 4mCl^- \quad (2a)$$

where $\{Au\}_m$ stands for a Au nucleus consisting of m atoms on the C(0001) surface. Later, nuclei further grow by incorporating Au atoms discharged either on the substrate or directly on the Au island surface according to

$$C(0001)\{Au\}_m + AuCl_4^- + 3e^- = C(0001)\{Au\}_{m+1} + 4Cl^- \quad (2b)$$

The standard potential of reaction 2b in the working solution is $E^\circ = 0.757$ V, and its isothermal temperature coefficient, $dE^\circ/dT = -0.63 \times 10^{-3}$ V/K.[13] In all cases, the cathodic current attains a limiting value (j_L) covering a relatively wide potential range.

For $T < 313$ K, the cathodic limiting current is preceded by a current hump typical of a mass-transport-controlled electrochemical reaction. The initial slope of the j vs E curve increases and the potential of the current hump shifts positively as T is increased.

The dependence of j_L on the $AuCl_4^-$ concentration c fits the equation for a mass-transport-controlled electrochemical process,[14]

$$j_L = zFD_i c/\langle\delta\rangle \quad (3)$$

$z = 3$ being the number of electrons per reactant ion in either reaction 2a or 2b, F the Faraday constant, $\langle\delta\rangle$ the average stationary diffusion layer thickness under free convection, and D_i the diffusion coefficient of the reactant species ($AuCl_4^-$) in

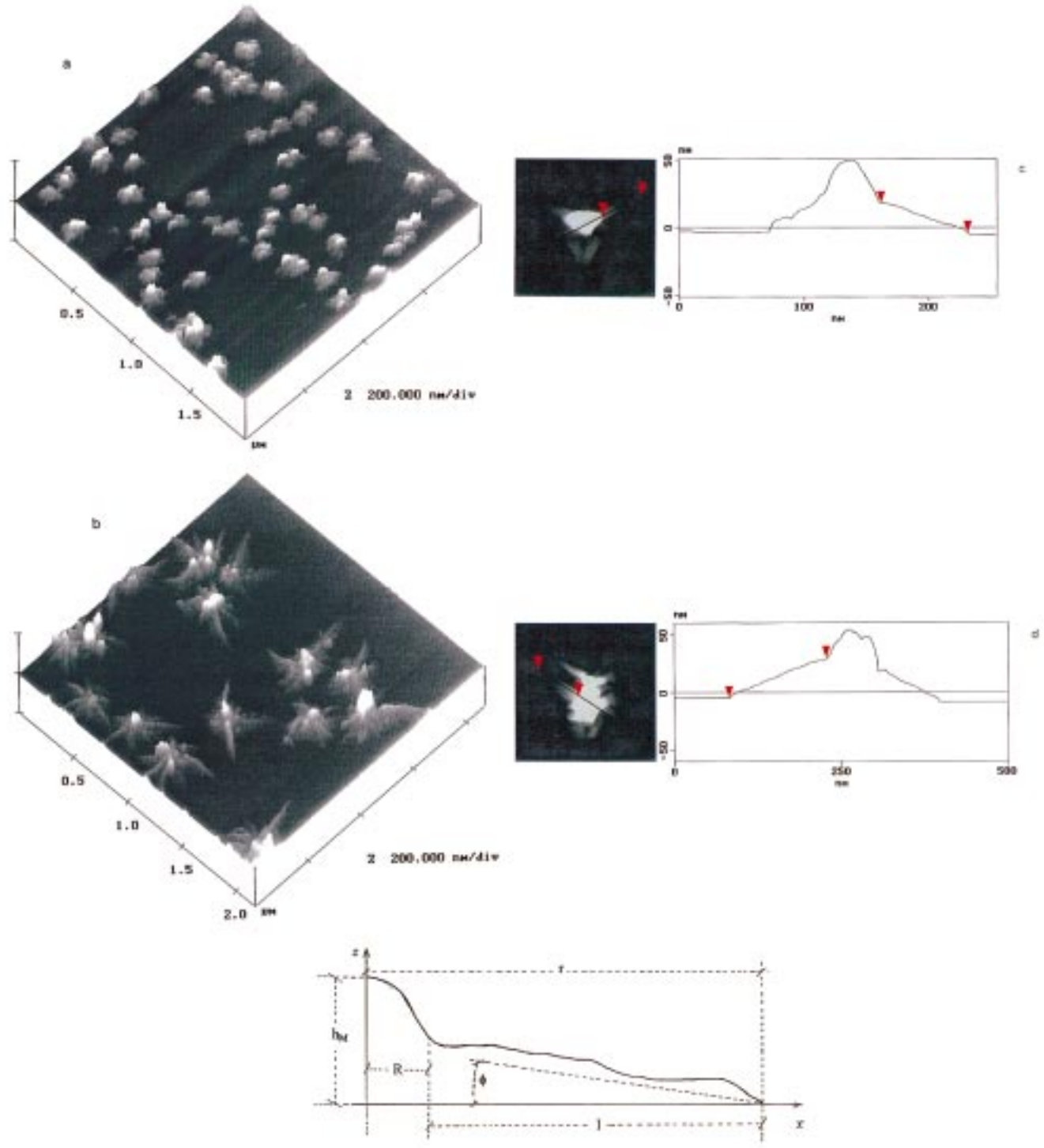

Figure 2. (a) and (b): Ex situ STM images (2×2 μm^2, topographic mode) of gold islands on C(0001) produced from aqueous 5×10^{-4} M $AuCl_3 \cdot HCl + 0.5$ M $NaClO_4 + 0.01$ M $HClO_4$ under constant flux, $q = 6$ mC/cm^2, $T = 275$ K, and $T = 298$ K, respectively. (c) and (d): Longitudinal cross sections from STM images for dendrites produced at $T = 275$ and 298 K, respectively. (e, bottom) A scheme (cross section) of the core (one-half) and dendrite branch of an island including geometric parameters used in the text.

the solution. According to eq 3, the value of j_L could be adequately adjusted by changing c.

The temperature dependence of j_L fits an Arrhenius plot, i.e., the ln j_L vs $1/T$ plot results in a straight line. From the slope of this line, the experimental activation energy for the overall electrochemical process results in $E^* = 3.8 \pm 0.2$ Kcal/mol. This figure is equal to E_D^*, the activation energy for the reactant diffusion in the solution.[14]

3.2. STM Imaging. Ex situ STM images of electrode surface domains resulting from $c = 5 \times 10^{-4}$ M and $q = 6$ mC/cm^2 at 275 K ($j_L = 0.04$ mA/cm^2) (Figure 2a) and $T = 298$ K ($j_L = 0.06$ mA/cm^2) (Figure 2b) show fractional coverage of the C(0001) substrate by randomly distributed Au islands of a rather uniform size and shape. Each island consists of a large number of tiny Au crystals with a high rounded central core and branches without tip splitting as expected for dendrites, emerging at 120°

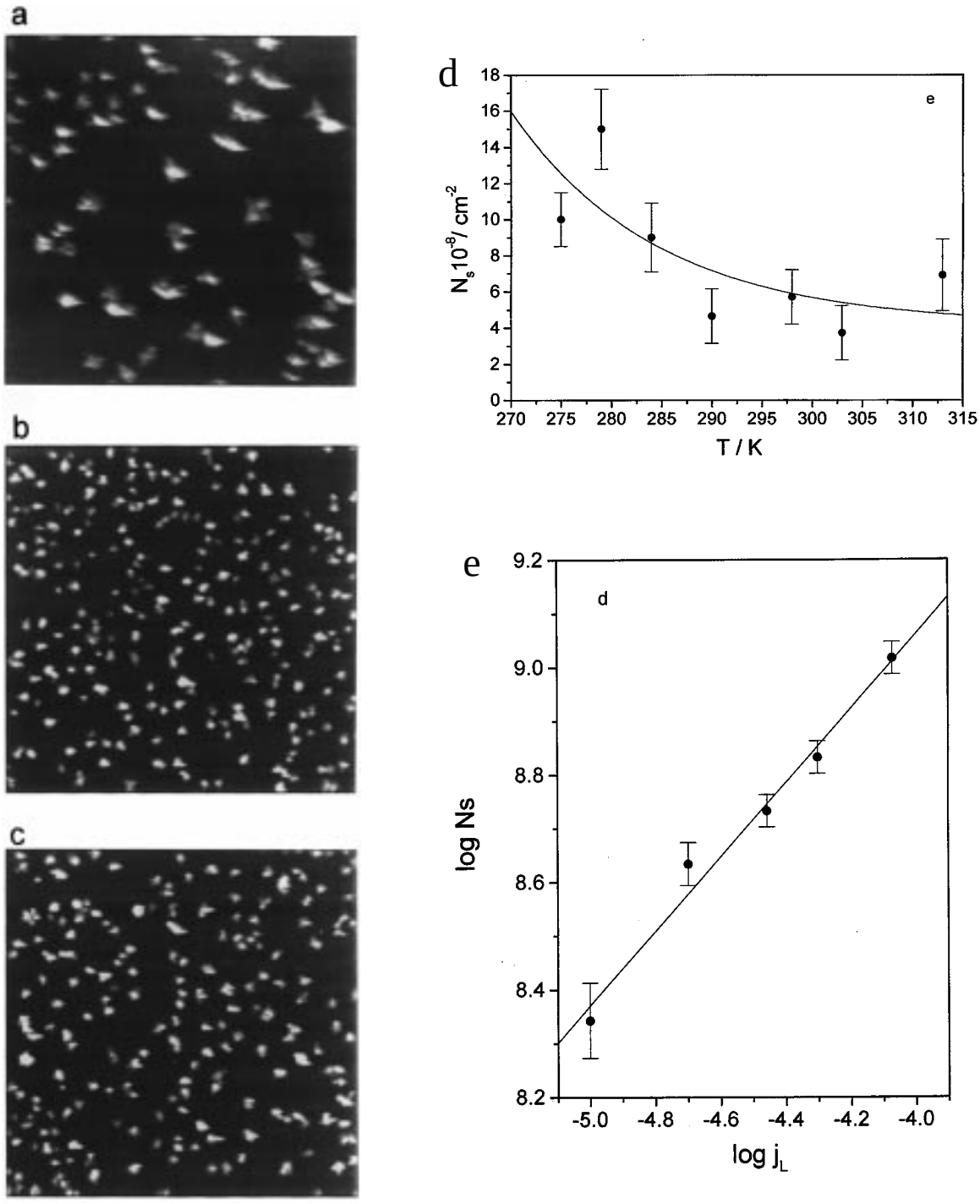

Figure 3. (a−c): Ex situ STM images (5×5 μm^2, topographic mode) of gold aggregates on C(0001) for $q = 6$ mC/cm^2, at different values of c and T. (a) $c = 5 \times 10^{-5}$ M, $T = 298$ K. (b) $c = 5 \times 10^{-4}$ M, $T = 275$ K, (c) $c = 5 \times 10^{-4}$ M, $T = 298$ K. (d) Log N_s vs log j_L plot for $q = 6$ mC/cm^2. The slope of the straight line is 0.69 ± 0.03. (e) N_s vs T plot from runs involving $q = 6$ mC/cm^2.

angles. These patterns are consistent with the formation of Au-(111) islands as reported elsewhere.[11] The longitudinal cross section of a single branch (Figure 2c,d) reveals a sequence of terraces decreasing in height from the core border toward the branch tip by one or two-atom high steps.

A cross section of a typical Au island along the direction of one branch (Figure 2e) can be described in terms of the length of the largest branch (l), the branch width (w), the branch slope (ϕ), and the maximum island height at the core (h_M) (Figure 2e). The value of l is measured from the radius of the core (R), and ϕ is defined as the average angle formed by the substrate plane and the branch surface plane measured from the tip. At constant E and q, all these parameters depend on T. Thus, for $c = 5 \times 10^{-4}$ M and $q = 6$ mC/cm^2, as T is increased from 275 to 313 K, ($\langle l \rangle$), the average value of l increases, in contrast to $\langle \phi \rangle$, the average value of ϕ (Figure 2c,d). The small values of $\langle \phi \rangle$, and the fact that $\langle l \rangle > \langle h_M \rangle$ indicate that for dendrite growth $d\langle l \rangle/dt > d\langle h_M \rangle/dt$. Otherwise, for a given q, the ratio $\langle l \rangle/\langle w \rangle$ becomes almost constant, irrespective of T.

Branched islands have also been observed for vapor-deposited Au on C(0001).[7,8] However, in this case, the island surface is essentially smooth with $\langle \phi \rangle \approx 0$.[15] The difference between the island surface of these deposits and that of electrodeposited Au islands on C(0001) can be explained by a different growth

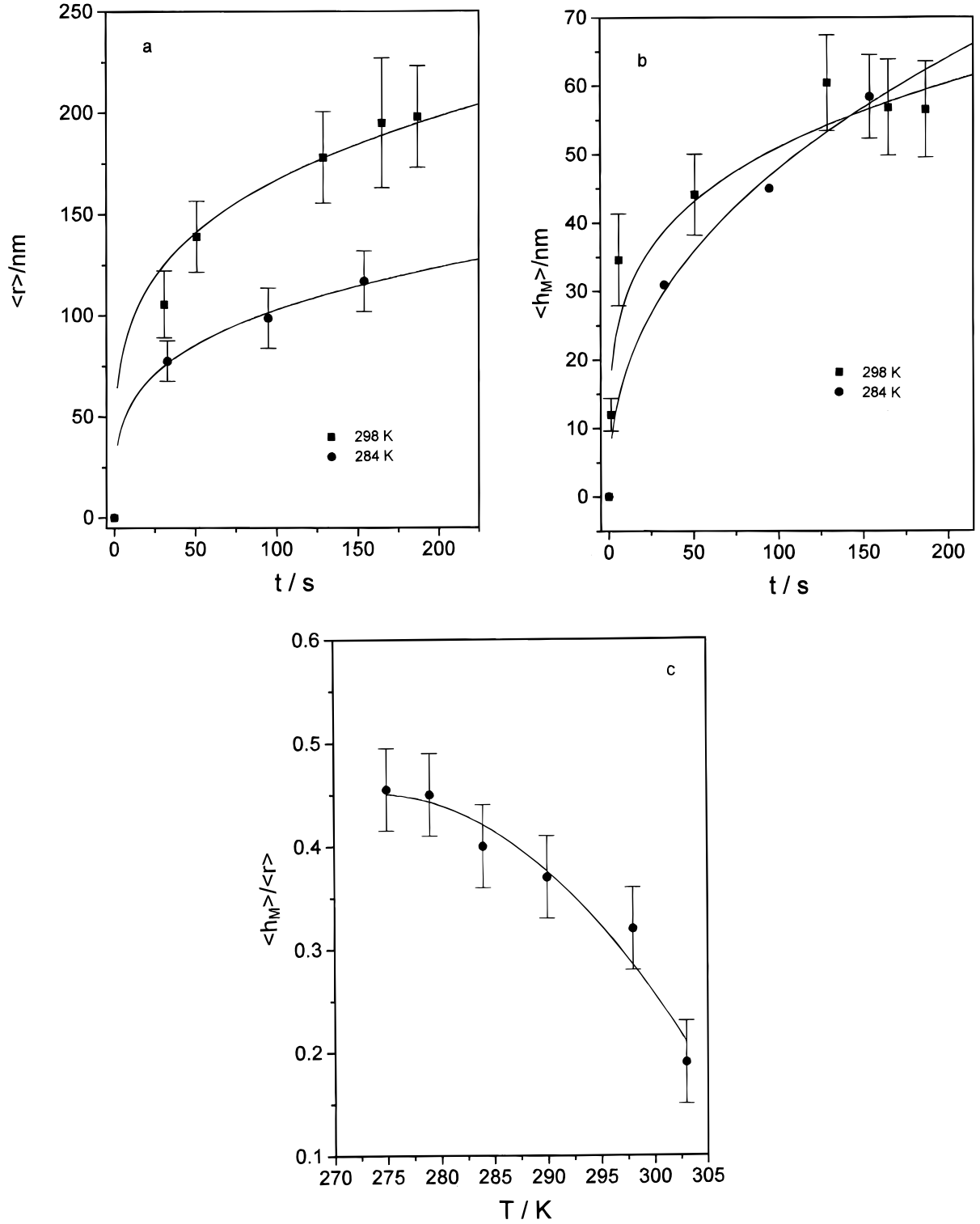

Figure 4. (a) Plots of $\langle r \rangle$ vs t for $T = 284$ K and $T = 298$ K. (b) Plots of $\langle h \rangle$ vs t obtained from gold dendritic branches produced at $T = 284$ K and $T = 298$ K. (c) Plot of $\langle h \rangle / \langle r \rangle$ vs T resulting from runs involving $q = 6$ mC/cm^2.

kinetics. Thus, the kinetics of vapor-deposited Au islands on C(0001) is determined by a surface reaction, whereas the electrodeposition of Au islands on the same substrate is governed by ionic mass transport from the solution side. In this case, growth normal to the substrate is enhanced at protrusions (island cores) leading to a nonzero slope between the central core and the branch tip.[1]

3.3. Density of Au Islands. The density of Au crystals (N_s) on C(0001) depends on both j_L and T (Figure 3a−c). Thus, at $T = 298$ K, N_s increases with j_L according to $N_s \propto {j_L}^X$ with $X = 0.69 \pm 0.03$ (Figure 3d). On the other hand, for $c = 5 \times 10^{-4}$ M and $q = 6$ mC/cm^2, N_s decreases exponentially with T (Figure 3e).

3.4. Size Evolution of Au Islands. Results from experiments run at different T and $c = 5 \times 10^{-4}$ M show that the average maximum radius ($\langle r \rangle$) enclosing each Au crystal obeys the kinetic law $\langle r \rangle \propto t^n$ with $n = 0.25 \pm 0.05$ (Figure 4a). This relationship is consistent with a growth process in which the surface diffusion of attaching particles plays a dominant role in the growth process.[16]

On the other hand, the average maximum value of island heights obeys a $\langle h_M \rangle \propto t^p$ relationship with a T-dependent value of p (Figure 4b), as p changes from 0.25 ± 0.05, for $T = 303$ K, to 0.50 ± 0.05 for $T = 275$ K (Figure 4b). The increase in p on decreasing T suggests a decrease in the diffusion length of those Au atoms directly discharged on the Au island surface. Accordingly, the $\langle r \rangle / \langle h_M \rangle$ ratio decreases as T is decreased from 313 to 275 K, assisting the formation of a rough pattern (Figure 4c).

3.5. Geometry of Au Islands. For all values of T and $q < 0.6$ mC/cm^2, Au islands can be described as compact quasi-spherical objects obeying a euclidean geometry. Conversely, for $q > 0.6$ mC/cm^2, branched islands with a fractal geometry are formed. These islands can be analyzed as 2D objects to evaluate their fractal dimension using the perimeter−area ($P-A$) method.[16] For this purpose, cross sections of each Au island parallel to the substrate plane at a given height (h_c) measured from the substrate surface are obtained from STM images. After repeating this procedure for a number of h_c values, a collection of 2D Au islands is obtained. The P vs A relationship fulfills the following proportionality:[17]

$$\log P \propto (D_f/2) \log A \tag{5}$$

where D_f is the dimension of the object. From the $P-A$ method, when $h_c \rightarrow 0$, all branches are included in the 2D island resulting in $D_f = 1.6 \pm 0.1$. Conversely, when $h_c \rightarrow h_M$, only the compact core of the island is analyzed and $D_f \rightarrow 1$, i.e., islands approach a euclidean behavior.

4. Discussion

4.1. Possible Contributions to the Electrochemical Growth of Au Islands on C(0001). The initial electrochemical growth of Au islands on C(0001) involves the transport of reactants from the solution to the C(0001) surface, their discharge at C(0001) defective sites[11] to form nuclei (reaction 2a), and nucleus growth producing randomly distributed islands (reaction 2b). In this growth process two stages, one for $q < 0.6$ mC/cm^2 and the other one for $q > 0.6$ mC/cm^2, can be distinguished. The first stage leads to compact Au islands, whereas the second results in branched Au(111) islands with $D_f = 1.6$.

Assuming that the discharge of Au ions on C(0001) is less efficient than that on Au,[11] branching will occur mainly by Au adatoms spilling over from the core region of each island to dendrite tips. This process should involve the diffusion of Au adatoms on smooth Au(111) terraces and from terrace to terrace across monoatomic steps (Figure 5a). It should be remembered that surface diffusion of adatoms on single crystal (111) faces is asymmetric leading to dendrite formation, owing to the existence of two different types of steps.[4−6] The terrace-to-terrace atom diffusion assists further branch growth and secondary branching.[11]

According to the above description, surface diffusion of Au adatoms on Au in the absence of energy barriers at step edges would produce perfect 2D smooth islands growing in the direction parallel to the C(0001) plane, whereas the existence of asymmetric energy barriers for terrace-to-terrace surface atom diffusion would produce dendrites and control the rate of island growth in the vertical direction. In this case, the values of D_f and $\langle l \rangle / \langle w \rangle$ ratio, and the $\langle r \rangle \propto t^{1/4}$ relationship, are T-independent, providing a sound indication that the mechanism of Au island branching on C(0001) remains the same over the range of T covered in this work.

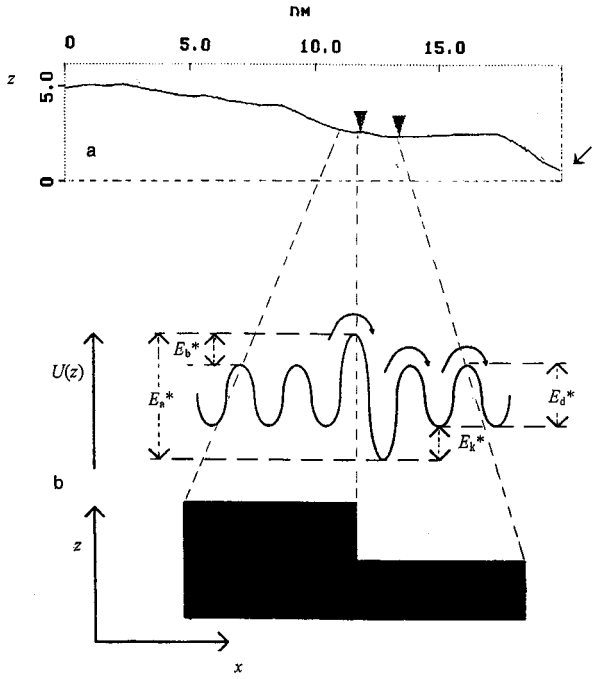

Figure 5. (a) Typical STM longitudinal profile of a gold dendritic branch electrodeposited on C(0001) from aqueous 5×10^{-4} M $AuCl_3$·HCl + 0.5 M $NaClO_4$ + 0.01M $HClO_4$ under constant flux, $q = 6$ mC/cm^2 and $T = 298$ K. The arrow indicates the dendrite tip. (b) Scheme of a single atom high step resulting from a. The different activation energy barriers to surface diffusion of gold atoms are indicated.

4.2. Driving Force and Possible Energy Barriers for Au Adatom Surface Diffusion. The rate of displacement of Au adatoms from the core to branch tips is determined by different energy barriers to adatom surface diffusion (Figure 5b). These barriers impose a constraint to the terrace-to-terrace Au adatom surface diffusion.[18]

Considering the topography of Au islands, the accumulation of Au atoms at the cores, is favored by the smaller local value of δ at protrusions for the ionic mass-transport-controlled electrochemical reaction.[11] Therefore, during Au electrodeposition the surface concentration of Au adatoms (c_{ad}) gradually changes from a maximum value at core regions to a practically null value at branch tips, so that the chemical potential gradient between the core region and branch becomes the driving force for surface diffusion. This fact implies that $(\Delta c_{ad})_M$, the maximum concentration difference of Au adatoms, becomes constant as its average value at the core surface ($\langle (c_{ad})_M \rangle$) is proportional to the constant flux of electrodepositing particles (j_L), and $\langle c_{ad} \rangle \Rightarrow 0$ at the branch tip. In fact, considering that the branch surface consists of a series of terraces of length l_{Ti}, decreasing in height from the central core towards the tip (Figure 2e), the overall driving force for Au adatom surface diffusion ($\Delta \mu_{ad}/\Delta l$) can be expressed as

$$\sum_{i=1}^{n} \partial \mu_{ad} / \partial l_{T_i} \rightarrow (\Delta \mu_{ad}/\Delta l) \tag{6}$$

where μ_{ad} and l_{T_i} denote the chemical potential of Au adatoms and the length of the ith terrace ($i = 1, 2, ..., n$), respectively. Taking into account that

$$(\Delta \mu_{ad}/\Delta l) \propto \Delta \ln c_{ad}/\Delta l \tag{7}$$

and

$$(\Delta c_{ad})_M/\Delta t \propto j_L \quad (8)$$

Then, it follows that,

$$j_L \propto v_r \propto (\Delta c_{ad})_M/\Delta l \quad (9)$$

According to relationship 9 v_r, the growth rate of the tip front in the branch direction, is proportional to the Au adatom concentration gradient in the same direction.

4.3. Kinetics of Dendritic Branching. Let us consider the growth of 2D circular Au islands under constant flux involving terrace-to-terrace adatom surface diffusion. Taking into account that the island radius (r), i.e. the characteristic length of the system, is given by the proportionality,[1]

$$r^4 \propto D_s/j_L \quad (10)$$

D_s being the surface diffusion coefficient of Au atoms on Au. The area (A_i) of the circular island fits the proportionality

$$A_i \propto r^2 \propto (D_s/j_L)^{1/2} \quad (11)$$

and for intermediate and high substrate coverage (Figure 3), the island density becomes

$$N_s \propto 1/r^2 \propto (D_s/j_L)^{-1/2} \quad (12)$$

Expression 12 can be written as

$$N_s/(j_L)^{1/2} \propto (D_s)^{-1/2} \quad (13)$$

Otherwise, the temperature dependence of D_s is given by[16]

$$D_s \propto e^{-E_a^*/RT} \quad (14)$$

Then, from eqs 13 and 14 the following proportionality holds

$$N_s/(j_L)^{1/2} \propto e^{E_a^*/2RT} \quad (15)$$

leading to a linear $\ln N/(j_L)^{1/2}$ vs T^{-1} plot with the slope $= E_a^*/2$.

The same analysis can be extended to dendritic islands ($D_f = 1.6$) resulting from terrace-to-terrace adatom surface diffusion towards branch tips involving the simultaneous shift of step edges and branch tips. In this case,

$$N_s/(j_L)^{0.63} \propto e^{0.63E_a^*/RT} \quad (16)$$

Then, at constant T, expression 16 predicts a linear N_s vs $(j_L)^{0.63}$ dependence that is very close to that resulting from experimental data (Figure 6). Therefore, from the slope of the ln (N_s/j_L^X) vs $1/T$ plot (Figure 6) the value $E_a^* \approx 11$ Kcal mol^{-1} is obtained. This figure is smaller than $E_a^* \approx 14$ Kcal mol^{-1}, which has been reported for Au atom surface diffusion in Cl^--ion-free acid solutions.[19] This difference, however, can be understood since the presence of Cl^- ions in the solution increases the surface mobility of Au adatoms. It is known that the adsorption of Cl^- ions decreases the Au−Au bond energy.[20,21]

5. Conclusions

(i) The ex situ STM topography of Au islands electrodeposited on C(0001) at constant flux under ionic mass transport control, in the range $275 < T < 313$ K, exhibits only a compact quasi spherical core for $q < 0.6$ mC/cm^2, and a core decorated with symmetrically distributed dendritic branching for $q > 0.6$ mC/cm^2. Dendritic islands behave as fractals with the dimension $D_f = 1.6$. (ii) The rate of displacement of branch tips measured from STM imaging data can be explained by a Au adatom surface diffusion mechanism. (iii) The driving force for the directional Au adatom surface diffusion is the quasi-steady chemical potential gradient established longitudinally along each branch from the island core to branch tip. (iv) From the temperature and flux dependences of island density, the energy barrier to Au-adatom surface diffusion results in $E_a^* \approx 11$ Kcal/mol.

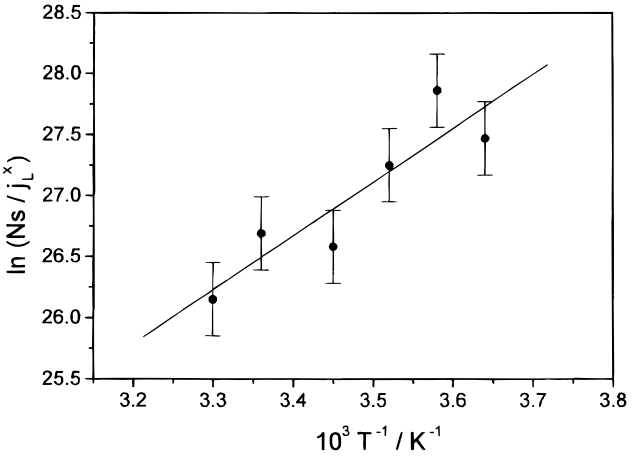

Figure 6. ln (N_s/j_L^X) vs T^{-1} plot. Data resulting from runs involving $q = 6$ mC/cm^2. The slope of the straight line leads to $E_a^* \approx 11$ Kcal/mol.

Acknowledgment. This work was financially supported by Project PB94-0592A (DGICYT), Spain, and PICT 97-1993 from Agencia Nacional de Promoción Científica y Tecnológica and Grant PIP 014/97 from Consejo Nacional de Investigaciones Científicas y Técnicas, Argentina.

Glossary

A	area resulting from the "islands and lakes"procedure used to determine D_f
A_i	area of circular island
ad	adatom
c	molar concentration of discharging ions
c_{ad}	molar concentration of adatoms
$\langle c_{ad} \rangle$	average molar concentration of adatoms
$(c_{ad})_M$	maximum molar concentration of adatoms
D_f	fractal dimension
DDA	deposition, diffusion and aggregation
DLA	diffusion limited aggregation
D_i	diffusion coefficient of ions in the solution
D_s	surface diffusion coefficient of adatoms
E	electrode potential
$E^{o,}$	standard electrode potential
E_{pzc}	potential of zero charge
E^*	experimental activation energy for transport of ions in the solution derived from electrochemical data
E_D^*	activation energy for the diffusion of reactive species in the solution
E_a^*	activation energy for adatom surface diffusion
F	Faraday constant
F	flux of depositing particles
HOPG	highly oriented pyrolitic graphite
h_M	maximum height at the island core
$\langle h_M \rangle$	average maximum height at the island core

h_c height of planes parallel to the substrate plane used in the P-A method to evaluate the fractal dimension

j apparent cathodic current density referred to the C(0001) surface area

j_L apparent cathodic limiting current density

k Boltzmann constant

l length of the largest dendrite branch

$\langle l \rangle$ average length of the largest dendrite branches

l_{Ti} length of the ith terrace

m number of atoms in a Au nucleus

N_s island density

n exponent in the $\langle r \rangle \propto t^n$ relationship

n number of terraces forming a dendritic branch

P perimeter resulting from the "islands and lakes"procedure used to determine D_f

p exponent at the $\langle h_M \rangle \propto t^p$ relationship

q apparent charge density related to gold electrodeposition

R island core radius

R universal gas constant

r maximum radius enclosing island

$\langle r \rangle$ average maximum radius enclosing island

SCE saturated calomel electrode

STM scanning tunneling microscopy

T temperature

t time

U potential energy

v electric potential scanning rate

v_r displacement rate of the dendrite tip

w width of a dendrite branch

X exponent in the $N \approx j_L^X$ relationship

x cartesian coordinate

z cartesian coordinate

z number of electrons per discharging ion

$\langle \delta \rangle$ average Nernst diffusion layer thickness

ϕ angle formed by the substrate plane and the upper dendrite plane

$\langle \phi \rangle$ average angle formed by the substrate plane and the upper dendrite plane

μ_{ad} chemical potential of adatoms

2D two dimensional

3D three dimensional

References and Notes

(1) Barabasi, A. L.; Stanley, E. In *Fractal Concepts in Surface Growth*; Cambridge University Press: Cambridge, 1995.

(2) Hwang, R. Q.; Schroder, J.; Gunther, G.; Behm, R. J. *Phys. Rev. Lett.* **1991**, *67*, 3279.

(3) Meakin, P. In *The Fractal Approach to the Heterogeneous Chemistry*; Avnir, D., Ed.; Wiley: New York, 1989, p 131 and references therein.

(4) Brune, H.; Roder, H.; Bromann, K.; Kern, K.; Jacobsen, J.; Norskov, J. *Surf. Sci*. **1996**, *349*, L115.

(5) Hohage, M.; Bott, M.; Morgenstern, M.; Zhang, Z.; Michely, T.; Comsa, G. *Phys. Rev. Lett*. **1996**, *76*, 2366.

(6) Mueller, B., Nedelman, L., Fischer, B., Brune, H., Barth, J., Kern, K. *Phys. Rev. Lett.* **1998,** *80*, 2645.

(7) Darby, T. P., Wayman C. M. *J.Cryst. Growth* **1975**, *28*, 41. Wayman, C. M.; Darby, T. P. *J. Cryst. Growth* **1975**, *28*, 53.

(8) Nishitani, R.; Kasuya, A.; Kubota, S.; Nishina, Y. *J. Vac. Sci. Technol*. **1991**, *B9*, 806.

(9) Heyraud, J. C., Metois, J. J. *J. Cryst. Growth* **1980**, *50*, 571.

(10) Budevski, E.; Staikov, G.; Lorenz, W. J., In *Electrochemical Phase Formation and Growth*; VCH: Weinheim, 1996.

(11) Martín, H.; Carro, P.; Hernández Creus, A.; González, S.; Salvarezza, R. C.; Arvia, A. J. *Langmuir* **1997**, *13*, 110.

(12) Hill, G. J.; Ives, J. G. In *Reference Electrodes*; Ives, D. G., Janz, G., Eds.; Academic Press: New York, 1961; Chapter 3, p. 127.

(13) Schmid, G. M.; Curley-Fiorino, M. E. In *Encyclopedia of Electrochemistry of the Elements*; Bard, A. J., Ed.; Marcel Dekker: New York, 1975; vol. IV, p 87.

(14) Glasstone, S.; Laidler, K. J.; Eyring, H. In *The Theory of Rate Processes*; McGraw-Hill: New York and London, 1941; Chapter 9, p 480; Arvia, A. J.; Marchiano, S. L. In *Los Fenómenos de Transporte en Electroquímica*; Comisión de Investigaciones Científicas: Provincia de Buenos Aires, 1971; Chapter 12, p 251.

(15) Blum, B. B.; Salvarezza, R. C.; Arvia, A. J. In preparation.

(16) Pimpinelli, A; Villain, J.; Wolf, D. E.; Metois, J.; Heyraud, J. C.; Elkinani, I.; Uimin, G. *Surf. Sci*. **1993**, *295*, 143.

(17) Gómez-Rodríguez, J. M.; Baró, A. M.; Vázquez, L.; Salvarezza, R. C.; Vara, J. M.; Arvia, A. J. *J. Phys. Chem*. **1992**, *96*, 347.

(18) Li, Y.; DePristo A. E. *Surf. Sci.* **1996**, *351*, 189.

(19) Alonso, C.; Salvarezza, R. C.; Vara, J. M.; Arvia, A. J.; Vázquez, L.; Bartolomé, A.; Baró, A. M. *J. Electrochem. Soc.* **1990**, *137*, 2161.

(20) Trevor, D. J.; Chidsey, C. E. D.; Loiacono, D. N., *Phys. Rev. Lett.* **1989**, *62*, 929.

(21) García, P.; Gómez, M.; Salvarezza, R. C.; Arvia, A. J. *J. Electroanal. Chem.* **1993**, *347*, 237.